Acosta, A.R., Luo, Y., Austin, J.M.: Simultaneous Fluid and Structure Measurements of an Impinging Shock-Boundary Layer Interaction in Mach 4 Flow. California Institute of Technology, Pasadena, CA, USA. Presented at the 35th International Symposium on Shock Waves (ISSW35), Brisbane, Australia, 05-14 July 2025.

Simultaneous Fluid and Structure Measurements of an Impinging Shock-Boundary Layer Interaction in Mach 4 Flow

Alex R. Acosta, Ying Luo, and Joanna M. Austin

California Institute of Technology, Pasadena CA 91125, USA
aacosta@caltech.edu

Abstract. An impinging shock turbulent boundary layer interaction (STBLI) over both rigid and compliant surfaces is experimentally investigated. Simultaneous diagnostic techniques including time-resolved full-field photogrammetry, high-speed schlieren, and focused laser differential interferometry measurements have been applied to capture both the fluid and structure response of the interaction. Modal analysis techniques revealed that surface compliance did not significantly affect the global structure of the shock motion but did result in a transfer of energy from the low-frequency STBLI unsteadiness to the compliant panel's fundamental vibration frequency. The separation shock was loosely phase-coupled with the reattachment shock at the panel fundamental frequency and generally led the reattachment shock motion by a quarter oscillation cycle. High frequency content in the boundary layer after flow reattachment exhibited at least a factor of two greater spectral energy in the compliant case compared to the rigid case.

Keywords: shock boundary layer interaction, fluid-structure interaction, focused laser differential interferometry, photogrammetry, schlieren

1 Introduction

A defining characteristic of separated shock wave turbulent boundary layer interactions (STBLI) over rigid walls is broadband low-frequency separation shock and separation bubble motion [1]. When surface compliance is introduced, the unsteady surface pressure loading associated with STBLI can excite multiple structural vibration modes, which can significantly modify the interaction dynamics through fluid-structure coupling. Structural oscillations can affect the size of the separation bubble, extent of the separation shock foot motion, and synchronization of the separation and reattachment point motion.

Similar to rigid wall interactions, several compliant surface impinging STBLI studies also observed that the separation shock foot motion is out of phase with the reattachment motion [2, 3]. Although Varigonda and Narayanaswamy found the separation shock foot motion to lag the reattachment motion at frequencies that do not coincide with panel vibration modes, they discovered that the separation and reattachment motions were highly synchronized at the panel vibration modes [4]. They conclude this synchronization is likely due to the spanwise

coherence of the separation shock at the panel modes, which creates spanwise coherent shear layer eddies that convect downstream and drive the reattachment shock motions. In contrast, D'Aguanno et al. observed that the separation shock motion lags the mode 1 panel oscillations by a quarter cycle [3].

The large parameter space and modeling complexity of these interactions necessitate more experiments to investigate the behavior of the fluid-structure coupling. The goal of this study is to conduct impinging STBLI experiments over a compliant surface while simultaneously measuring the fluid and structure responses. Photogrammetry, schlieren, and focused laser differential interferometry (FLDI) measurement techniques are leveraged to capture panel surface deformation, shock motion, and separation bubble and boundary layer dynamics. Two of our previous STBLI studies conducted in the Caltech Ludwieg tube revealed that surface compliance alters the shape of the separated region and enhances the streamwise extent of the separation shock foot unsteadiness [5, 6]. This study is carried out in collaboration with the groups of Profs. McNamara and Gaitonde at The Ohio State University.

2 Experimental Setup

2.1 Facility & Model

Experiments were conducted in the Caltech Ludwieg tube operating at Mach 4 with air as the test gas. The Caltech Ludwieg tube generates approximately 60 ms test time of steady Mach 4 flow. For this test campaign, all experiments were performed at one set of flow conditions, listed in Table 1.

Table 1: Flow conditions.

M_∞	p_{res} [kPa]	p_∞ [kPa]	u_∞ [m/s]	T_∞ [K]	ρ_∞ [kg/m^3]	Re [m^{-1}]
4	250	1.53	667	69	0.0770	1.03×10^7

The experimental model for this work is the same as used in a previous study conducted by Acosta and Austin [6]. The STBLI is generated by a 35° wedge shock generator rotated 10° downward mounted above a flat plate model with interchangeable rigid and compliant panel inserts. The oblique shock formed by the shock generator impinges on the panel insert approximately mid-chord. The compliant panel insert is made from $h = 0.254$ mm thick 316 stainless steel and is clamped on all sides to an aluminum base via epoxy (Loctite E-60HP). The compliant area of the panel is $a = 53.3$ mm long in the streamwise direction and $b = 78.7$ mm wide in the spanwise direction.

Underneath the compliant panel is a 50.6 mm deep pressure controlled cavity that is pressurized to $p_c = 4.25p_\infty$. This cavity pressure nearly corresponds to

the average pressure STBLI load over the panel during test time. Prior to flow arrival, the panel center point is deflected approximately one panel thickness upward due to the pressure difference.

A 25.4 mm wide strip of coarse sand paper mounted 12.7 mm downstream of the flat plate leading edge trips the boundary layer to ensure it is fully turbulent over the panel. The incoming visual boundary layer thickness at the leading edge of the compliant surface ($x/a = -0.5$) is measured to be $\delta_0 = 3.3$ mm.

2.2 Diagnostics

Full-field panel deflection measurements are obtained using a high-speed, single-camera photogrammetry setup. This non-intrusive technique tracks the displacement of surface painted markers on the compliant panel. A custom MATLAB script identifies the centroids of each imaged marker, and a bundle adjustment routine converts the centroid coordinates from the two-dimensional camera coordinate systems to the three-dimensional global coordinate system. Additional details of this photogrammetry system are provided by Acosta and Austin [6].

Fluid measurements are simultaneously recorded using a colinear FLDI and high-speed schlieren system. The high sensitivity and temporal resolution of FLDI make it particularly effective in resolving density fluctuations within the turbulent boundary layer and separation bubble. Complementary full-field schlieren visualization is employed to capture the structure and unsteady dynamics of the shock motion. A schematic of the optical setup for all three measurements is provided in Fig. 1, and additional specifications of this colinear FLDI and schlieren system are given in Luo et al. [7]. For this study, the schlieren images are illuminated by a Cavilux HF 640 nm pulse diode laser at a 20 ns pulse width and recorded by a Phantom v2512 high-speed camera at a 100 kHz sampling rate. The photogrammetry images are illuminated by four continuous white light emitting diodes and recorded by a Phantom v1612 high-speed camera at a 10 kHz sampling rate. The photogrammetry and schlieren images are synchronized by a Berkeley Nucleonics 577 pulse generator. The FLDI signal is measured by a Thorlabs PDA36A2 photodetector at a 1 MHz sampling rate.

3 Results and Discussion

Snapshots of the time-resolved flow field and panel deformation data are shown in Fig. 2 for a full panel oscillation cycle at vibration mode (1,1). The black rectangle in the x-y plane represents the panel boundary, the red-blue colormap visualizes the panel vertical displacement, and the grayscale image is the captured schlieren image.

The panel oscillates for around 32 periods at its first vibration mode during test time. The time- and trial-averaged panel center point deflection is $\bar{z}_{center}/\delta_0 = -0.0167$, and the trial-averaged root mean square of the center point fluctuations is $\mathrm{RMS}\{z'_{center}/\delta_0\} = 0.0080$. The frequency content of the center point and point at ($x/a = -0.19$, $y/b = -0.11$) are analyzed in a power

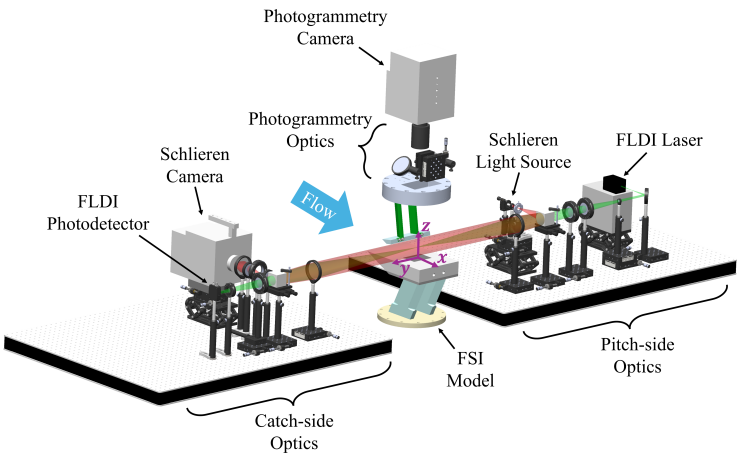

Fig. 1: Schematic of experimental model and diagnostic setup.

spectral density plot in Fig. 3. The latter point is chosen to not lie on any nodes of the lowest order vibration modes. Both the center and nodeless points exhibit a strong peak at the first vibration mode frequency, $f_{(1,1)}$, that has almost two orders of magnitude greater energy than the next leading peak. This signifies that vibration mode (1,1) dominates the panel response in this interaction. Notably, a small bump below $f_{(1,1)}$ at a frequency between 250 to 450 Hz is present in the power spectra and corresponds to the low-frequency STBLI unsteadiness. Six additional panel vibration modes are detected using proper orthogonal decomposition (POD) on the panel deflection data, and their frequencies are identified by dashed lines in Fig. 3. Modes (1,3) and (2,1) share nearly identical frequencies, which are indistinguishable in the power spectra. Additionally, the time-averaged panel deflection shape resembles mode (2,1) due to the STBLI surface pressure load, which is strongest in the downstream half of the panel.

3.1 Schlieren Feature Tracking

The streamwise positions of the separation and reattachment shocks, $x_{SS}(z,t)$ and $x_{RS}(z,t)$, are tracked in each schlieren frame using a threshold edge detection method. Similarly, the visual boundary layer height, $z_{BL}(x,t)$, is tracked downstream of flow reattachment. The time-averaged shock and boundary layer positions are overlaid on the schlieren snapshots in Fig. 2. Only minimal differences between the rigid and compliant cases are observed in the root mean square values of shock motion, as seen in Table 2. The root mean square of the separation shock motion is roughly three times as large as that of the reattachment shock motion for both rigid and compliant cases.

POD is also employed on the tracked separation and reattachment shock positions to decompose the motion into the highest energy mode shapes, $\Phi_i(z)$, and temporal coefficients, $\psi_i(t)$. The POD mode shapes and corresponding mode

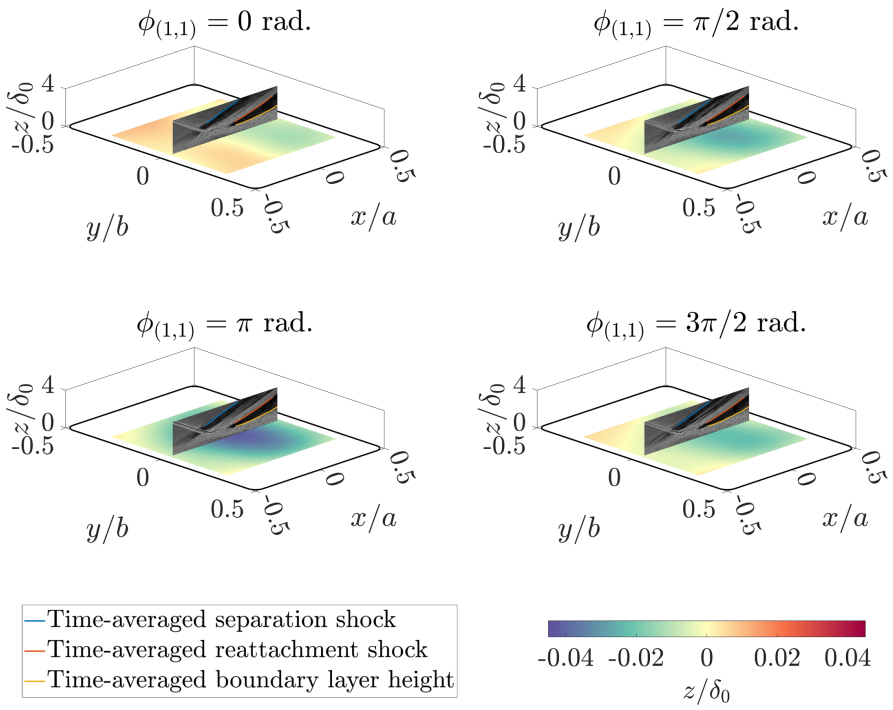

Fig. 2: Simultaneous schlieren and photogrammetry snapshots for a full panel oscillation cycle at vibration mode (1,1). Time-averaged shock and boundary layer positions are overlaid on schlieren snapshots. Flow is in the $+x$-direction.

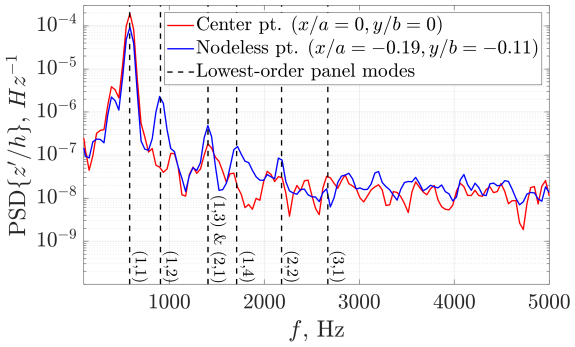

Fig. 3: Power spectra of panel response at center point and nodeless point.

energies for the compliant case are shown in Fig. 4. For both the separation and reattachment shocks, mode 1 corresponds to a curve that is nearly parallel to the time-averaged shock position. The separation shock mode 1 energy is

Table 2: Root mean square of shock fluctuations.

	Rigid case	Compliant case
RMS$\{x'_{SS}(z/\delta_0 = 2.7)/a\}$	0.0265	0.0271
RMS$\{x'_{RS}(z/\delta_0 = 1.7)/a\}$	0.0096	0.0092

close to 90%, which signifies that a majority of the shock motion is captured by the first POD mode. Consequently, this means that within the measured vertical range of $z/\delta_0 = 2.33$ to 3.06, the phase of the separation shock motion is roughly equivalent, and, therefore, the entire shock is displaced upstream and downstream uniformly.

In contrast, the reattachment shock mode 1 energy is close to 70%, which signifies that higher order mode contributions are more significant in the reattachment shock motion. Mode 2 has about 19% energy and corresponds to a curve that crosses the time-averaged shock position once. Mode 3 has close to 9% energy and crosses the time-averaged shock position twice. This result implies that the reattachment shock does not solely shift upstream and upstream uniformly, but instead has additional rotational/bending motion. Therefore, the reattachment shock motion is more complex and cannot be solely represented by mode 1 unlike the separation shock motion.

Interestingly, the rigid case POD mode shapes and energies are nearly identical to those of the compliant case shown in Fig. 4. The rigid case separation shock POD mode energy is 89.6%, and reattachment shock POD mode 1 energy is 69.3%. This result suggests that surface compliance does not significantly affect the global structure of the shock motion compared to the rigid case.

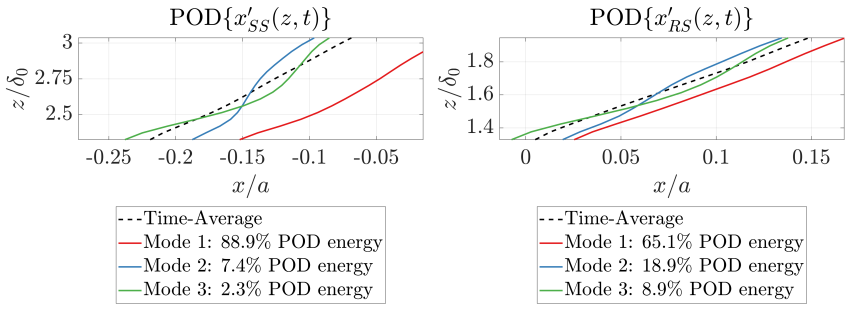

Fig. 4: Compliant POD modes of separation and reattachment shock motion.

Spectral proper orthogonal decomposition (SPOD) is also applied to the tracked shock positions to identify the frequencies of oscillation with the highest energy content. The SPOD mode 1 energy spectra for the separation and

reattachment shocks and boundary layer are shown in Fig. 5. For the rigid case separation shock motion, there is a strong broadband peak centered around 300 Hz, which corresponds to the low-frequency STBLI unsteadiness. Surface compliance attenuated this low-frequency unsteadiness and transferred energy at the panel vibration mode (1,1) frequency, $f_{(1,1)}$, to the separation shock. Similarly, the reattachment shock and boundary layer also have distinct peaks at $f_{(1,1)}$ in the compliant case. The energy at $f_{(1,1)}$ is nearly one order of magnitude greater than the energy at all other frequencies in the reattachment shock motion. Notably, there is also greater energy within the low frequency unsteadiness range in the boundary layer motion of the compliant case compared to that of the rigid case.

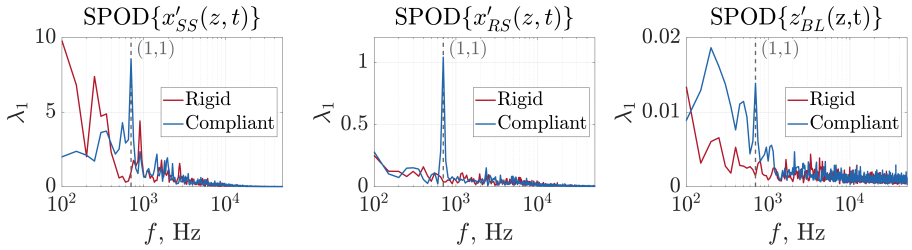

Fig. 5: Leading SPOD mode energy of separation shock, reattachment shock, and boundary layer motions.

3.2 Phase Analysis

Time-averaged phase behavior between the separation shock and reattachment shock at $f_{(1,1)}$ is estimated using cross-spectral analysis. The phase-locking value (PLV) between the two signals is also computed to quantify the phase difference consistency over time (Eq. 1). A PLV close to 1 signifies that the signals are strongly phase coupled while a PLV close to 0 signifies that there is no consistent phase synchronization.

The phase difference between the separation shock and reattachment shock at $f_{(1,1)}$ ($\Delta\phi_{SS,RS}$) for each repeated compliant experiment is plotted in Fig. 6. On average, the separation shock tends to lead the reattachment shock motion by a quarter panel oscillation cycle with a moderate degree of phase-locking (trial-averaged $\text{PLV}_{SS,RS} = 0.53$). Repeated experiments show relatively good agreement in both average phase difference and phase-locking value. The limited strength of the phase-coupling may be attributed to the nonlinear nature of the interaction, the contribution of higher order panel modes, or the fact that the separation and reattachment shock motions are measured off-surface slightly above the boundary layer and separation bubble.

$$PLV_{A,B} = \left| \frac{1}{N_{images}} \sum_{j=1}^{N_{images}} e^{i(\phi_A(t_j) - \phi_B(t_j))} \right| \tag{1}$$

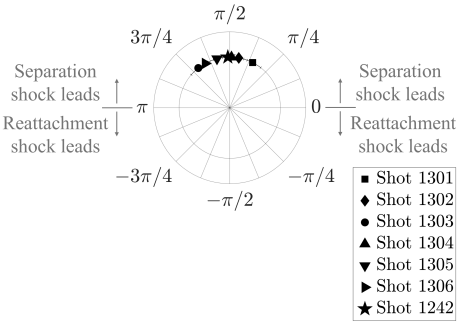

Fig. 6: Phase difference between the separation and reattachment shock at $f_{1,1}$. The leading POD temporal coefficient, $\psi_{1_{SS}}(t)$, represents the separation shock motion, and the streamwise shock position at $z/\delta_0 = 1.7$ represents the reattachment shock motion.

3.3 FLDI Results

Density fluctuations in the incoming boundary layer, separation bubble, and boundary layer after reattachment are investigated using FLDI with beam pairs oriented parallel to the wall. Power spectra of the FLDI responses are computed using the background noise subtracted method outlined by Lawson [8], and the results are shown in Fig. 7. The incoming boundary layer features a broadband peak centered around 120 kHz. After flow reattachment, the energy content in the boundary layer is increased by nearly an order of magnitude across all frequencies. In both the rigid and compliant cases, the broadband peak is decreased to approximately 70 kHz. This decrease has also been observed by previous compression ramp and impinging STBLI studies [9, 10].

The energy content within the separation bubble is elevated and relatively flat around 5 to 20 kHz. This medium frequency range is likely associated with shear layer vortices convecting over the separation bubble [9]. Notably, the compliant case separation bubble spectra has lower overall energy content than the rigid case spectra. However, this could be due to differences in FLDI beam pair height above the wall rather than differences in interaction dynamics. In the rigid case, as the height above the wall increases, the overall energy content also increases. This trend is also present in the boundary layer as well. Though, the compliant case exhibited greater energy content in the boundary layer after reattachment compared to the rigid case. The compliant power spectra at $z/\delta_0 = 0.51$ has

roughly twice the energy than the rigid power spectra at $z/\delta_0 = 0.66$. Therefore, surface compliance does not alter the high frequencies present in the boundary layer but does increase the overall energy content.

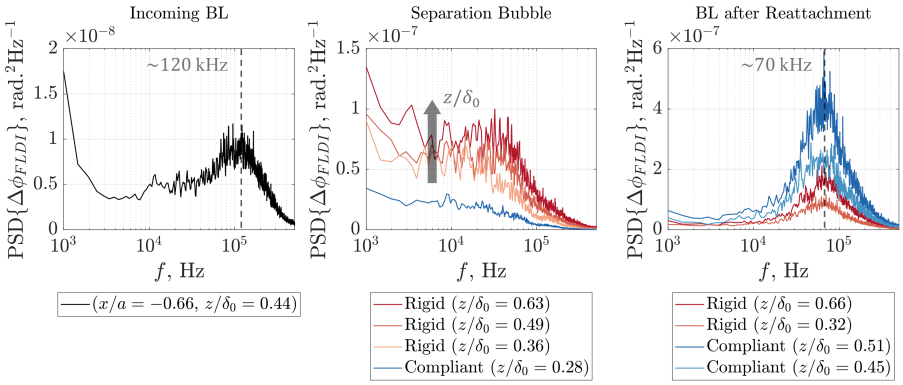

Fig. 7: Power spectra of FLDI response.

4 Conclusion

Simultaneous fluid and structure measurements of an impinging STBLI over both rigid and compliant surfaces were captured and analyzed in the present study. The compliant panel response was dominated by mode (1,1) oscillations, and the time-averaged panel deflection shape resembled mode (2,1). Root mean square values and POD analysis of the shock motion revealed that surface compliance did not significantly alter the global structure of the separation and reattachment shock motion. However, there was a significant transfer of energy in the separation shock motion from the low-frequency STBLI unsteadiness to the panel's mode (1,1) vibration frequency, $f_{(1,1)}$, based on the leading SPOD mode energy spectrum. The reattachment shock and boundary layer after flow reattachment also exhibited strong peaks at $f_{(1,1)}$ in the compliant case. The separation and reattachment shocks were loosely phase-coupled at $f_{(1,1)}$, with the separation shock typically leading the reattachment shock motion by a quarter panel oscillation cycle. Lastly, density fluctuation measurements within the boundary layer after flow reattachment showed that surface compliance increased the overall spectral energy by at least a factor of two but did not shift the broadband peak present in the rigid case. Additional regions in the flow field will be probed by FLDI in future experiments to uncover more insights into the interaction dynamics. Future studies will also examine the fluid-structure coupling behavior using nonlinear analysis techniques and will investigate the effect of shock impingement location on the fluid and structure response.

5 Acknowledgments

This work is supported in part by the Air Force Office of Scientific Research under Award No. FA9550-22-1-0063, subaward from The Ohio State University, with Dr. Sarah Popkin and Dr. Amanda Chou as program officers, and by the National Science Foundation Graduate Research Fellowship under Grant No. DGE-1745301. The authors would like to thank Ali Kiani and Noel Esparza-Duran for assistance fabricating parts for the experimental setup. Additionally, the authors thank Wesley Yu, Michael Stramenga, and Joel Lawson for their technical knowledge and assistance.

References

1. Clemens, N.T., Narayanaswamy, V.: Low-Frequency Unsteadiness of Shock Wave/Turbulent Boundary Layer Interactions. Annual Review of Fluid Mechanics 46, 469-492(2014). doi:10.1146/annurev-fluid-010313-141346
2. Musta, M.N., Ahn, Y.J., Eitner, M.A., Sirohi, J., Clemens, N.T.: Unsteadiness in Shock/Boundary-Layer Interaction Over a Compliant Panel at Mach 2. In: AIAA AVIATION Forum. AIAA (2022). doi:10.2514/6.2022-4136
3. D'Aguanno, A., Allerhand, P.Q., Schrijer, F.F.J., van Oudheusden, B.W.: Characterization of shock-induced panel flutter with simultaneous use of DIC and PIV. Experiments in Fluids. 64(15), (2023). doi:10.1007/s00348-022-03551-1
4. Varigonda, S.V., Narayanaswamy, V.: Fluid structure interactions generated by an oblique shock impinging on a thin elastic panel. Journal of Fluids and Structures 119 (2023). doi:10.1016/j.jfluidstructs.2023.103890
5. Neet, M.C., Austin, J.M.: Effects of Surface Compliance on Shock Boundary Layer Interaction in the Caltech Mach 4 Ludwieg Tube. In: AIAA SCITECH 2020 Forum. AIAA (2020). doi:10.2514/6.2020-0816
6. Acosta, A.R., Austin, J.M.: Experimental Investigation of an Impinging Shock-Boundary Layer Interaction on a Compliant Panel in Mach 4 Flow. In: AIAA SCITECH 2024 Forum. AIAA (2024). doi:10.2514/6.2024-1153
7. Luo, Y., Acosta, A.R., Austin, J.M., Hornung, H.G.: Co-linear Focused Laser Differential Interferometry and High Speed Schlieren Measurements of Supersonic Cylinder Near Wake. In: 35th International Symposium on Shock Waves. (2025).
8. Lawson, J.M.: Focused Laser Differential Interferometry. PhD diss., California Institute of Technology (2021). doi:10.7907/5thh-f652
9. Dupont, P., Haddad, C., Deviéve, J.F.: Space and time organization in a shock-induced separated boundary layer. Journal of Fluid Mechanics 559, 255-277(2006). doi:10.1017/S0022112006000267
10. Helm, C.M., Martín, M.P., Williams, O.J.H.: Characterization of the shear layer in separated shock/turbulent boundary layer interactions. Journal of Fluid Mechanics 912, A7(2021). doi:10.1017/jfm.2020.989